# Dose-Free Monitoring of Radiotherapy Treatments With Scattered Photons: Concept and Simulation Study

Micaela Cunha, Marco Pinto, *Member, IEEE*, Hugo Simões, *Member, IEEE*, Brígida Ferreira, Maria do Carmo Lopes, Paulo Fonte, and Paulo Crespo, *Member, IEEE*

***Abstract*—Modern radiotherapy (RT) techniques provide increasingly higher conformality, a potential invaluable clinical benefit to the patient. Consequently, in both single and multi-fractionated RT, patient misalignments and changing internal anatomy are also becoming more critical since higher conformality may equally represent a higher risk of target underdosage or organ-at-risk overdosage. Even with rigid fixation devices, maximum positioning errors higher than 1 cm are observable. In addition, anatomical morphological variations induced by cardiorespiratory or bowel motion, or RT-related biological responses, have been reported. The latter include tissue swelling, edema, inflammation, tumor shrinkage/growth, or filling of body cavities with unaccounted mucus or edematous tissue. State-of-the-art image-guided radiotherapy (IGRT) aims at providing feedback to the radiation oncologist in regard to these matters, some times at the cost of increased dosage (e.g. kilo and megavoltage IGRT), other times providing insufficient clinical information. We investigate a novel imaging system specially designed for monitoring both conventional and intensity/volumetric modulated photon radiotherapy (IMRT/VMRT, static and dynamic). The proof-of-principle and feasibility of such system indicate its potential for monitoring each field (and segment, for IMRT/VMRT) during all treatment fractions without whatsoever additional dose. We present a clear 2D correlation between the dose delivered in a heterogeneous phantom and the number of scattered photons detected perpendicular to the photon beam. Simulations of high-energy, multi-hole collimators show real-time, high-detectability of abnormal (though possible) irradiation scenarios with pertinent target morphological alterations, such as tumor dislocation or formation of edematous tissue.**

***Index Terms*—Compton scattering, dosimetry, gamma-ray cameras, medical imaging, Monte Carlo simulation, radiation imaging, real time systems, therapy.**

Manuscript received May 31, 2012; revised February 04, 2013 and April 27, 2013; accepted May 23, 2013. Date of publication June 19, 2013; date of current version August 14, 2013. The work of P. Crespo was supported by FCT-Fundação para a Ciência e a Tecnologia, Lisbon, Portugal, with grant no. SFRH/BPD/39223/2007 and the work of H. Simões was partly supported by an INOV.C grant co-funded by QREN, under the Mais Centro Program and the European Regional Development Fund. M. Cunha and M. Pinto contributed equally to this work

M. Cunha and M. Pinto were with LIP-Laboratório de Instrumentação e Física Experimental de Partículas, 3004-516 Coimbra, Portugal, they are now with IPNL-Lyon-Institut de Physique Nucléaire de Lyon, 69622 Villeurbanne Cedex, France (e-mail: micaela.cunha@coimbra.lip.pt; marco.pinto@coimbra.lip.pt).

H. Simões is with LIP-Laboratório de Instrumentação e Física Experimental de Partículas, 3004-516 Coimbra, Portugal (e-mail: hugo.simoes@coimbra.lip.pt).

B. Ferreira is with I3N-Institute of Nanostructures, Nanomodelling and Nanofabrication, Departamento de Física, Universidade de Aveiro, 3810-193 Aveiro, Portugal (e-mail: brigida@ua.pt).

M. C. Lopes is with IPOCFG, E.P.E. Instituto Português de Oncologia de Coimbra Francisco Gentil, 3000-075 Coimbra, Portugal (e-mail: mclopes@ipocoimbra.min-saude.pt).

P. Fonte is with LIP-Laboratório de Instrumentação e Física Experimental de Partículas, 3004-516 Coimbra, Portugal and also with ISEC-Instituto Superior de Engenharia de Coimbra, 3030-199 Coimbra, Portugal (e-mail: fonte@coimbra.lip.pt).

P. Crespo is with LIP-Laboratório de Instrumentação e Física Experimental de Partículas, 3004-516 Coimbra, Portugal and also with the Physics Department of the University of Coimbra, 3004-516 Coimbra, Portugal (e-mail: crespo@lip.pt).

Color versions of one or more of the figures in this paper are available online at http://ieeexplore.ieee.org.

Digital Object Identifier 10.1109/TNS.2013.2265159

## I. Introduction

HANDLING single- and multiple-fraction radiotherapy (RT) requires extreme care to guarantee maximum dose exposure to the tumor and minimum healthy-tissue dosage so to limit undesirable side-effects. Nevertheless, several physical and biological mechanisms disturb that precision requirement to an unknown and unpredictable extent. Examples of such RT-disturbing imprecisions range from patient mispositioning (maximum positioning errors higher than 1 cm are observable [1]), to anatomical morphological changes occurring during the course of treatment [2], [3] (e.g. tissue swelling due to edema or inflammation [4], tumor shrinkage, and/or filling of initially air-filled cavities). These and other morphology-changing factors [5] constitute the main challenge to the development of modern RT techniques. Consequently, it is desirable to detect and quantify such dose-changing mechanisms. This knowledge would allow the improvement of RT clinical outcomes by continuously supporting the medical doctor in its decision to: (1) stop and re-plan a given treatment that has evolved to a situation that does not fulfill the initial dose assumptions, or (2) continue the treatment with reassured quality. State-of-the-art technology aiming at this task is named image-guided radiation therapy (IGRT).

### A. Rationale for Dose Verification in Photon Radiotherapy

The use of information obtained from images is crucial in any type of radiotherapy. It can be useful either in the diagnosis phase, in the treatment planning, for monitoring the accuracy of dose delivery, and finally for monitoring the response to treatment [5], [6]. Dose verification assumes particular relevance in this process since during delivery any type of intra- or inter-fraction deviations relatively to the planning computed tomogram

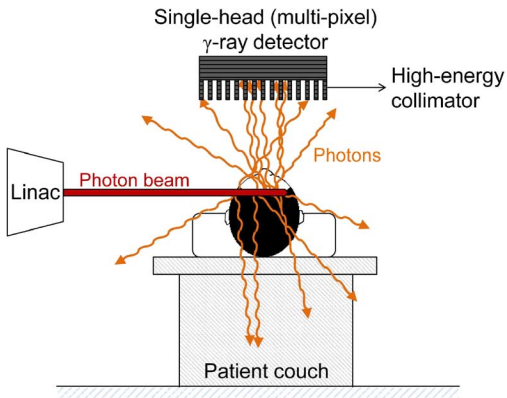


Fig. 1. Implementation of the monitoring system into a clinical RT environment. The photon beam coming from a linear accelerator (linac) interacts with the target (e.g. patient) and photons scattered at approximately right angles with the beam direction are collimated and collected by one or more detector heads.

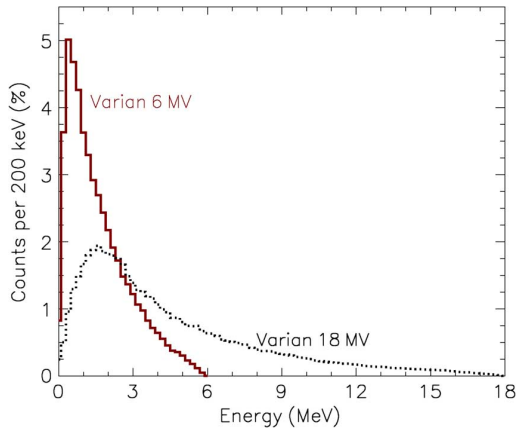


Fig. 2. Differential distributions of the two spectra with endpoint energies of 6 MeV and 18 MeV implemented into Geant4. The 6-MV linac energies are typically used for head-and-neck IMRT treatments, whereas the 18-MV energies are used for irradiation of the trunk (e.g. lung tumors).

may reduce the effectiveness of the treatment and may cause severe patient complications. In the case of photon RT different methods have been and are being developed to assess such patient variations, namely ultrasound, optical surface tracking systems, implantable electromagnetic markers, megavoltage X-ray electronic portal imaging (EPI), and in-room megavoltage (MV) or kilovoltage (kV) X-rays [5], [7], [8]. Other imaging methods like magnetic resonance imaging (MRI) or positron emission tomography (PET) may also be used [5], [6]. The process in which deviations of patient repositioning and anatomy from the initial planning computed tomogram are detected and corrected for, if needed, is called adaptive radiotherapy (ART), in contrast to conventional static radiotherapy in which the treatment planning is based on one single computed tomogram and delivered to the patient throughout all fractions [1].

Fast 2D image-guided techniques have been available since the 80's with the integration of portal imaging devices in linear accelerators (linac) [9]. However, these cannot generally be used to visualize soft tissue [6], thus providing only bony structures deviations. Consequently, any anatomical deformations, organ movement or tumor response during treatment cannot be accounted for. Three-dimensional IGRT, with or without functional tumor information, becomes then an essential step in the treatment process and even more when new treatment techniques are delivered. With intensity modulated radiation therapy (IMRT) highly irregularly-shaped dose distributions with steep dose gradients in the tumor borders can be produced [3], [10], [11]. Cone-beam computed tomography (CBCT) tools produce a 3D online patient representation [8]. Using this technology, daily 3D in vivo dosimetry has been investigated and it is becoming standard practice in some clinical centers [12], [13]. Alternative solutions include CT or MRI scanners inside the treatment rooms [10], [14] or integrated in the linac [15]. Each of these techniques has its imaging potentialities and limitations, with potential side effects due to extra-dosage in both MV and kV CBCT.

For moving targets like lung tumors, 4D gating and tracking solutions are under development [16] or already under clinical use [17]. Several systems based on feedback mechanisms that enable online adaptation of the radiation delivery are becoming available [18]. Also, new methods for *in vivo* dosimetry based on the physical interactions occurring during irradiation are being tested like the in-beam PET applied to photon RT. This is based on the emission of positrons produced by photoneutron reactions [19]. However, the technique is mainly applicable for photon energies above 20 MeV (i.e., above the endpoint energies of most linacs).

None of the aforementioned techniques is able to provide a complete answer to the quest of detecting the dose-changing mechanisms. The present work investigates by detailed simulation a novel gamma-camera-like system capable of monitoring photon radiotherapy by searching in real time for convenient, dose-correlated radiation escaping the patient during each treatment. In particular, the main goal of this work consists in analyzing whether the physical information obtained from photons escaping at 90° from an irradiated phantom is correlated with the deposited dose. In addition, we also investigate if a first tentative target morphological alteration (edema) can be detected with this system.

It must be stated that other important uses of Compton scatter measurements were attempted before for imaging purposes [20]–[22]. The novelty of this work lies in its first time attempt to use Compton scattering for therapy monitoring.

## II. Concept

### A. Principle of Operation: High-Energy Multi-Hole Collimation

The implementation of the proposed monitoring system in a clinical RT environment is depicted in Fig. 1. A single, or multiple, detector-head is positioned at right-angle(s) with the beam direction (only one detector head shown in the image). Each detector head accepts photons that are scattered in the target only if they are emitted also at approximately right angles with the beam direction.

## III. Materials and Methods

All simulations were performed using the Geant4 toolkit [23], [24], version 9.4, and the emstandard_opt3 physics list

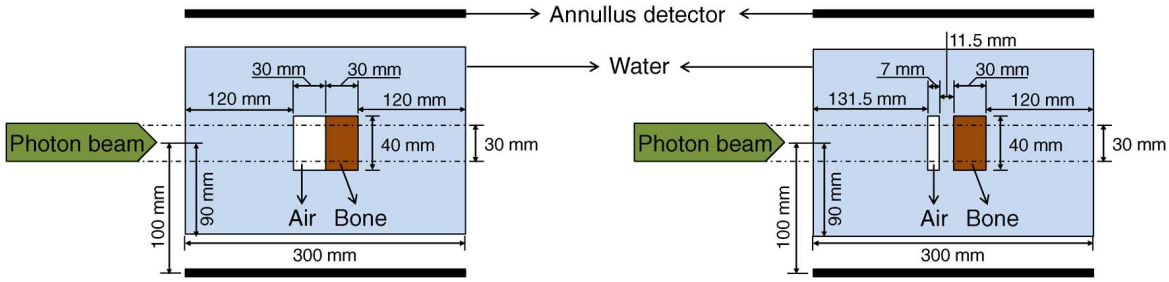


Fig. 3. Schematic side view of the simulated phantoms. **Left**: Normal. **Right**: Morphological alterations: air cavity partially filled with water.

(only electromagnetic processes were activated). In order to gain a first insight into the potentialities of the proposed monitoring system we have simulated some possible treatment scenarios.

The first approach to test this concept was to use a 30-mm-diameter photon beam with no divergence impinging on a cylindrical, heterogeneous target phantom. The shape of the beam spectra is depicted in Fig. 2 and was adapted from [25]. Most linacs in current use have two endpoint energies of 6 and 15 or 18 MeV. For this reason we have implemented into Geant4 the energy spectra of a linac from Varian Medical Systems [25] with endpoint energies of 6 MeV and 18 MeV. The 6 and 18-MV photon spectra were used in the first studies pertaining to Sections III-B-1 and III-B-2. For the studies with a fully-deployed, multi-hole collimation system (Section III-B-3) only the 6-MV photon spectrum was simulated.

### *A. Geant4 Dose Validation*

In order to validate the physics list implemented in Geant4, the longitudinal dose profile delivered into a homogeneous phantom made of water was simulated. The phantom consists of a cylinder with 90-mm radius and 300-mm length. The divergent beam used has a cross section of 40 mm $\times$ 40 mm at the isocenter, and an endpoint energy of 6 MeV (Varian 6 MV profile in Fig. 2). The simulated, longitudinal dose profile obtained was compared with the measured dose profile published in [26]. The dose profile was calculated by collecting, on a step-by-step basis within the Geant4 Monte Carlo, the energy deposited in the phantom. To compute the dose, this energy was then divided by the corresponding density and volume of the appropriate target (water in this case; water, bone, or air in the following sections).

### *B. Geant4-Based Heterogeneous Phantom*

Two different phantoms, depicted in Fig. 3, were used. Both consist of a 90-mm-radius water cylinder with a cylindrical-shaped air cavity and cortical bone inserted in it. The purpose of such phantoms is to mimic a human head, with the cortical bone representing a tumor, and in which the scattered radiation must traverse an amount of tissue-like material before escaping into the perfect detector.

*1) Normal Irradiation:* The phantom depicted in Fig. 3 (left) represents what was considered to be a normal irradiation. A cylindrical-shaped, 30-mm-long air cavity is positioned proximal to a 30-mm-long piece of cortical bone. Both the air cavity and the cortical bone have a diameter of 40 mm. A cylindrical-shaped perfect detector surrounding the phantom (Fig. 3) was used as target in a first-stage analysis. (Sections III-B-1 and III-B-2). This allows for a comparison to be made between longitudinal dose profiles and profiles obtained with detected photons. The term *perfect detector* refers to a solid or surface defined in Geant4. Every particle hitting such detector is stored in list mode format for further analysis such as e.g. optimum acceptance angle and energy threshold. In this case, photons were collected on the detector surface with an acceptance angle $\theta_{acc}$ given by $89.3^\circ \leq \theta_{acc} \leq 90.7^\circ$.

*2) Irradiation With Morphological Alterations:* The phantom depicted in the right image in Fig. 3 represents an irradiation scenario with morphological modifications. Namely, the length of the air cavity is reduced to 7 mm in respect to the normal irradiation. The purpose of this configuration is to emulate the partial filling of the initially air-filled cavity with mucus or edematous tissue.

*3) Fully Collimated System:* The concept of the proposed monitoring system relies on using photons that scatter in the phantom and reach the detector with approximately right angles in respect to the beam direction. For this, the implementation of a multi-hole collimator system is required. In order to test the feasibility of this concept, we have introduced a fully-collimated system built of lead into Geant4. Fig. 4 represents the front view of such a generic multi-hole collimator. Several multi-hole collimators (hexagonal holes) with different geometrical parameters, such as collimator thickness, septa distance (i.e., distance between two consecutive holes), and face-to-face distance (i.e., distance between two opposite faces of the hexagon) were simulated. The collimator front face, i.e., the face that is looking at the phantom, was always fixed at a distance of 280 mm from the beam central axis. The initial approach for designing these collimators was based on the work by Gunter [27]. We used those equations only as a first approach in order to collimate photons with nominal energies of 200, 300, 400, 500, 600, and 800 keV. The resulting parameters are summarized in Table I. A plane perfect detector built in Geant4 was positioned behind the multi-hole collimator, allowing the 2D image sampled with that detector to be seen. In addition, a longitudinal profile was computed along the direction $Z$. The integration in $X$ (perpendicular to the beam axis) for this profile is limited to $-15\ \mathrm{mm} \leq X \leq 15\ \mathrm{mm}$ since that is the width of the penetrating photon beam. This longitudinal profile of photon counts

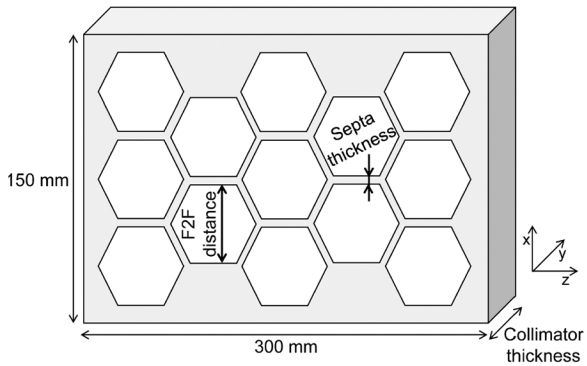


Fig. 4. Scheme of a hexagonal, multi-hole collimator. Parameters such as collimator thickness, septa thickness and face-to-face distance were manipulated in order to develop different collimators for different photon energies.

TABLE I
GEOMETRICAL PARAMETERS FOR EACH ENERGY COLLIMATOR COMPUTED ACCORDING TO [27]

| Energy (keV) | Collimator thickness (mm) | Septa thickness (mm) | Face-to-face distance (mm) |
|---|---|---|---|
| 200 | 45.912 | 0.12763 | 0.96548 |
| 300 | 80.811 | 0.31217 | 1.5349 |
| 400 | 116.99 | 0.52669 | 2.0196 |
| 500 | 151.40 | 0.73275 | 2.4051 |
| 600 | 182.93 | 0.91566 | 2.7080 |
| 800 | 237.43 | 1.2104 | 3.1445 |

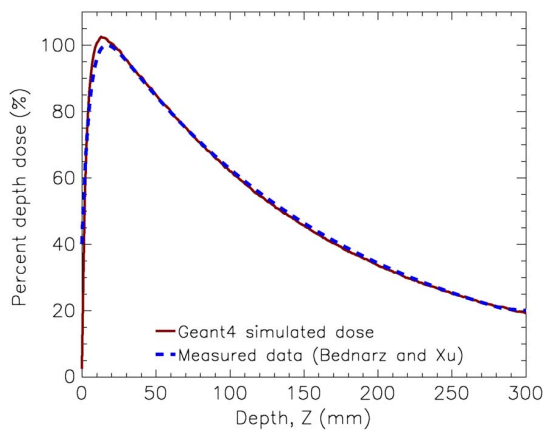


Fig. 5. Comparison between the dose profile simulated by Geant4 (brown, solid line) and a measured dose profile (blue, dashed line) [26]. A homogenous water phantom irradiated with a divergent, 6-MV beam with a cross section of 40 mm × 40 mm at isocentre was used in the simulation.

was normalized to the average dose in the tumor (bone), with the longitudinal dose profile also being shown.

## IV. RESULTS

### A. Geant4 Dose Validation

Fig. 5 shows the comparison between the Geant4 simulated longitudinal dose profile (brown, solid line) and a measured dose profile (blue, dashed line) published in [26]. This figure was constructed in accordance with a different published experiment [26] with the sole purpose of validating the simulation code in respect to dose profiles. The visual correlation verified between both profiles is very good, with a minor difference near the entrance to the phantom.

### B. Geant4-Based Heterogeneous Phantom

*1) Normal Irradiation:* The left column in Fig. 6 shows results obtained by irradiating the normal phantom with an 18-MV (top) and 6-MV (bottom) photon beam. In each plot the dashed, brown curve represents the longitudinal dose profile, whereas the solid, blue curve shows the yield of photons reaching the perfect detector with $89.3^\circ \leq \theta_{acc} \leq 90.7^\circ$. This photon yield is quantified as the ratio of the number of photons detected on each slice of the perfect, annular detector over the initial number of photons simulated out of the linac spectrum $(6 \times 10^9 \text{ photons})$.

*2) Irradiation With Morphological Alterations:* The right column in Fig. 6 shows results corresponding to an abnormal irradiation both with 18-MV photons (top) and with 6-MV photons (bottom). The difference of dose profiles obtained between the normal irradiation (left column in Fig. 6) and the irradiation under morphological alterations (right column in Fig. 6) are depicted in Fig. 7. The maximum percentage bone tumor underdosage is 5.6% and 9.3% for the 18-MV (left) and 6-MV irradiation (right), respectively. In addition to showing the maximum tumor underdosage, the figure also shows that the bone tumor suffers an almost-constant underdosage throughout its longitudinal extension in the $Z$ axis. Although it is the tumor underdosage that correlates with probability of tumor relapse, tumor overdosage is also a (legal) problem. The maximum tumor overdosages for the 18-MV and 6-MV irradiation were 94% and 68%, respectively.

*3) Fully Collimated System:* Figs. 8 through 11 show the results obtained with four hexagonal, multi-hole collimators implemented in Geant4 in order to discriminate photons with nominal energies of 400 (Fig. 8), 500 (Fig. 9), 600 (Fig. 10), and 800 keV (Fig. 11). The top plot in each figure shows the 2D photon count distribution arriving to a perfect detector positioned in the plane behind each multi-hole collimator. The dimensions of each collimator were presented in Table I. In the bottom plots in Figs. 8 through 11 (6-MV irradiation only) the corresponding depth-dose profiles (brown, dashed curve) along with the integral of the photon counts in the perfect detector occurring in the range $-15 \text{ mm} \leq X \leq 15 \text{ mm}$ (blue, solid curve) are shown. Similar collimators for nominal photon energies typical of nuclear medicine scenarios (gamma camera, single photon emission computed tomography—SPECT) were also studied (200 and 300 keV) but the plots are not shown because such collimators yield very poor correlation with the dose profiles. Table II presents the root mean square error (RMSE) and the correlation $R$ between the dose and the scattered photons detected with each energy collimator. Regarding the correlation test, a 95% confidence interval was used to assess the statistical information and for all cases a statistical significance of $p < 0.001$ was found.

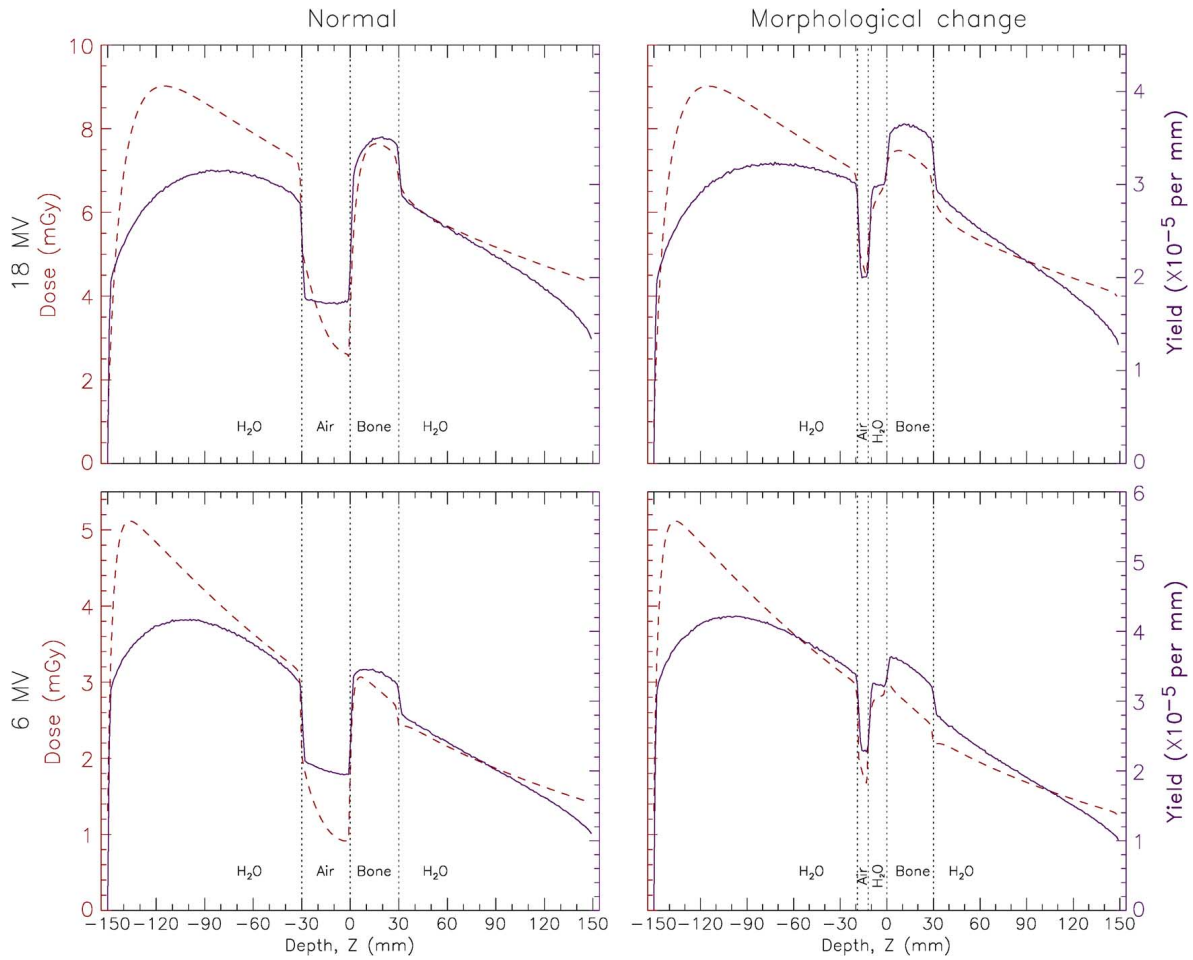


Fig. 6. Comparison between depth-dose profiles (brown, left Y-axis, dashed line) and collimated photon profiles (blue, right Y-axis, solid line). The angle of acceptance, defined as the angle $\theta_{acc}$ between the beam axis and the direction of each photon incident onto the perfect detector in Fig. 3, was set to $89.3° \leq \theta_{acc} \leq 90.7°$ in all images. **Top left**: Irradiation of a bone tumor located between 150 and 180-mm depth (Fig. 3, left) with an 18-MV photon beam. **Top right**: Edematous tissue fills 11.5 mm of each cavity wall, as depicted in the right image in Fig. 3. The morphological changes presented yield a maximum tumor underdosage of 5.6% (Fig. 7, left). **Bottom left**: same as above, but irradiation with a 6-MV photon beam. **Bottom right**: same as above, but now yielding a maximum tumor underdosage of 9.3%. In both cases the profiles of the photons that arrive to the perfect detector provide enough information allowing to discriminate between both irradiation scenarios (left and normal, from right and abnormal).

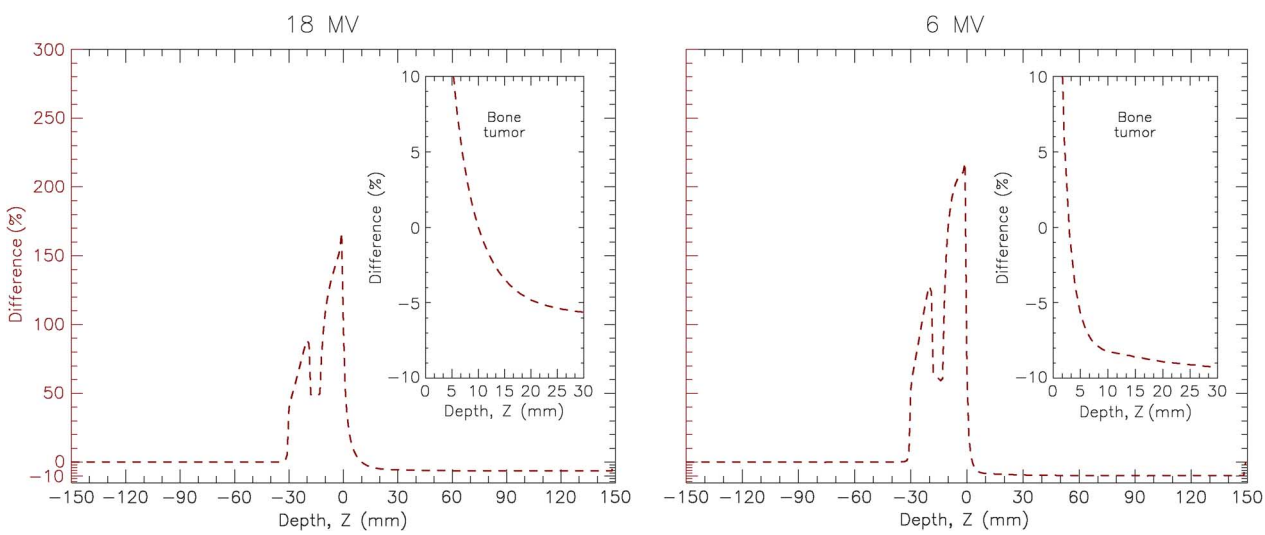


Fig. 7. Dose difference profiles obtained between the normal irradiation and the irradiation under morphological alterations depicted in Fig. 6. **Left**: Dose difference profile for the 18-MV case (top row in Fig. 6). **Right**: Dose difference profile for the 6-MV case (bottom row in Fig. 6).

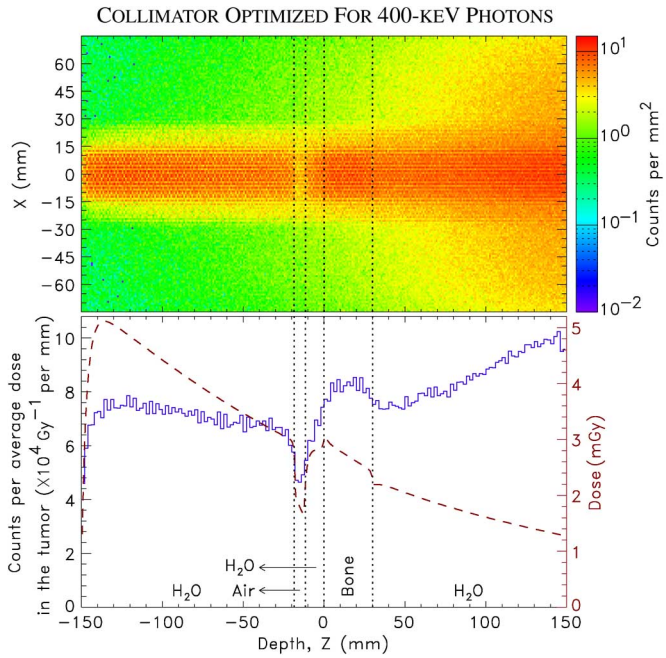


Fig. 8. Results obtained with a hexagonal multi-hole collimator designed for 400-keV photons [27]. **Top**: Two-dimensional distribution of photon counts hitting a perfect detector positioned behind the collimator. **Bottom**: Simulated depth-dose profile in the phantom (brown, dashed curve), together with the integral of the number of photon counts detected (blue, solid curve) within $-15\ \text{mm} \leq X \leq 15\ \text{mm}$ in the perfect detector, shown along the $Z$ axis.

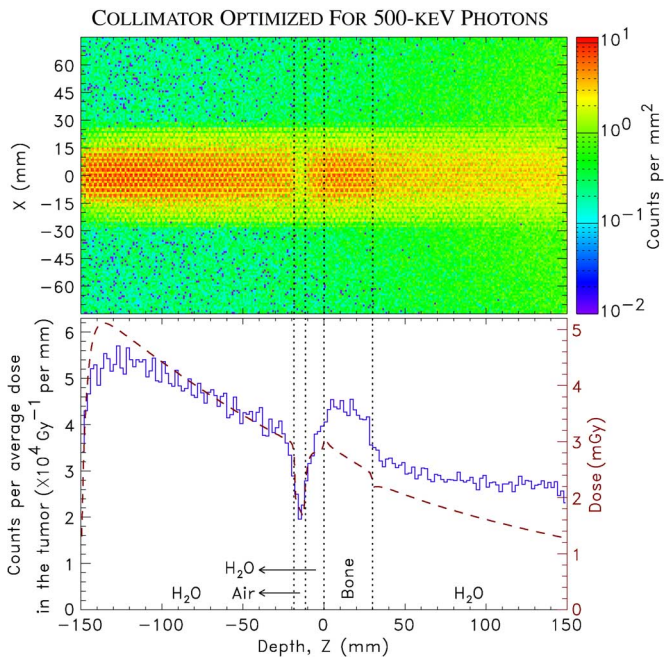


Fig. 9. Results obtained with a hexagonal multi-hole collimator designed for 500-keV photons [27]. **Top**: Two-dimensional distribution of photon counts hitting a perfect detector positioned behind the collimator. **Bottom**: Simulated depth-dose profile in the phantom (brown, dashed curve), together with the integral of the number of photon counts detected (blue, solid curve) within $-15\ \text{mm} \leq X \leq 15\ \text{mm}$ in the perfect detector, shown along the $Z$ axis.

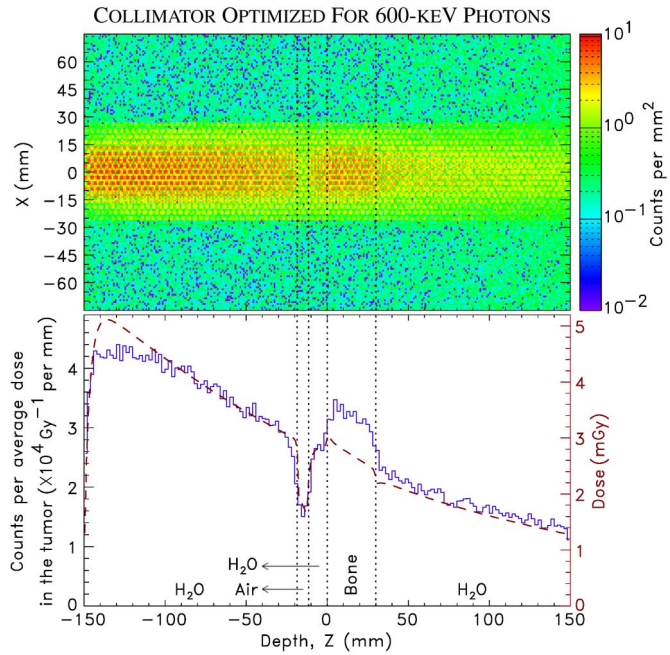


Fig. 10. Results obtained with a hexagonal multi-hole collimator designed for 600-keV photons [27]. **Top**: Two-dimensional distribution of photon counts hitting a perfect detector positioned behind the collimator. **Bottom**: Simulated depth-dose profile in the phantom (brown, dashed curve), together with the integral of the number of photon counts detected (blue, solid curve) within $-15\ \text{mm} \leq X \leq 15\ \text{mm}$ in the perfect detector, shown along the $Z$ axis.

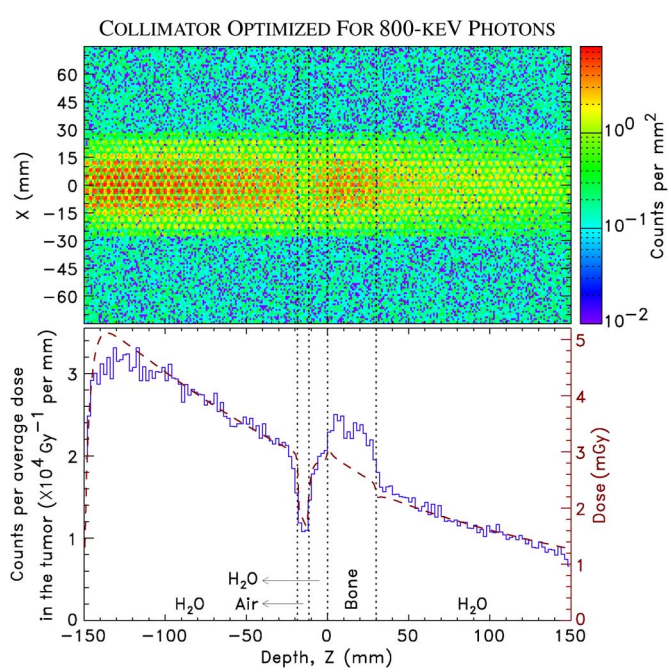


Fig. 11. Results obtained with a hexagonal multi-hole collimator designed for 800-keV photons [27]. **Top**: Two-dimensional distribution of photon counts hitting a perfect detector positioned behind the collimator. **Bottom**: Simulated depth-dose profile in the phantom (brown, dashed curve), together with the integral of the number of photon counts detected (blue, solid curve) within $-15\ \text{mm} \leq X \leq 15\ \text{mm}$ in the perfect detector, shown along the $Z$ axis.

TABLE II
RESULTS OF THE STATISTICAL TESTS [28] ASSESSING THE RELATION BETWEEN THE DOSE DATA AND THE NUMBER OF DETECTED PHOTONS IN THE PERFECT DETECTOR PLACED BEHIND THE HEXAGONAL-HOLES OF EACH MULTI-HOLE COLLIMATOR. ENERGY REFERS TO THE OPTIMIZED COLLIMATION ENERGY ACCORDING TO [27]. RMSE REFERS TO THE ROOT MEAN SQUARE ERROR

| Energy (keV) | RMSE | Correlation ($R$) between dose and detected photons profiles |
|---|---|---|
| 200 | 10813.15 | -0.9430 |
| 300 | 2143.04 | -0.9029 |
| 400 | 319.24 | -0.4749 |
| 500 | 119.91 | 0.9308 |
| 600 | 110.78 | 0.9442 |
| 800 | 94.03 | 0.9324 |

An analysis of the results presented in Table II makes it possible to conclude that, for hexagonal holes, the dimensions utilized in the collimator designed for a nominal photon energy of 600 keV yield the best dose-correlated results.

## V. DISCUSSION

We have so far considered the physics in a heterogeneous target phantom in great detail. This included normal and abnormal conditions (target with morphological alterations).

We have shown (Fig. 6) that both 6-MV and 18-MV photon irradiation allows for the profiles of the photons that arrive to the perfect detector to provide sound information in respect to a normal and abnormal (target with morphological alterations) irradiation scenario. The same conclusion may be drawn even when using a complete collimation system based on multiple, hexagonal-shape holes. Figs. 10 and 11 show that photons emerging from a heterogeneous phantom and passing through such a full collimated system do correlate with dose delivery (Table II). That table shows that the best correlation between the dose and the number of detected gammas occurs for the collimator designed for 600 keV, although the collimators designed for 500 keV and 800 keV also show fairly good correlation values. In addition, the dose in the bone tumor represented in the more realistic case depicted in Figs. 8 through 11 (6-MV irradiation only) is $\sim$3 mGy in all cases. This is quite a subtherapeutic value since the dose of IMRT beamlets, for example, starts at about 25 mGy, which is a factor 8 higher. These results provide good reasons for pursuing the implementation of such system for assisting external beam photon radiotherapy, potentially allowing for improvements in quality assurance of RT treatments. The fact that the events used for image construction are promptly collected renders the method fully insensitive to dynamical, biological mechanisms. Furthermore, the mathematics utilized for the construction of the dose-correlated photon depth-profiles is straightforward, requiring no iterative computation and, consequently, presenting no artifacts or distortions whatsoever, a potential advantage of this imaging system.

It must be finally stated that the images shown in Figs. 8 through 11 reveal that momentum conservation allows quite a number of photons dispersed in the forward direction to be collected if the face-to-face distance of the collimator holes is too large (Figs. 8 and 9). Reducing that parameter (face-to-face hole distance) strongly improves image quality by reducing such forwardly peaked photons (Figs. 10 and 11). The same can be seen in Fig. 6, which represents data collected with a perfect detector positioned in much closer proximity with the target. Consequently, a larger number of photons emitted in the forward cone is collected at larger penetration distance Z due to momentum conservation. In fact, an image obtained with a perfect collimator located at 210 mm from the phantom edge (not shown) reveals indeed a smaller influence of such forward-emitted photons.

## VI. CONCLUSIONS

The outcomes of this simulation work show that there are potentialities in the proposed monitoring system concerning RT treatment verification (including dose). The system shows potential to be able to detect morphological variations in real time and without whatsoever additional dose imparted to the patient. These results, together with the corresponding experimental measurements by Simões *et al.* [29], give a real insight of the capabilities that such system could have in clinical practice, both for treatment monitoring as well as for dosimetric verifications, potentially strongly complementing the information provided by other IGRT and ART techniques.

The dose simulated in the 6-MV scenario studied in this work is at least a factor eight smaller than minimum doses typically utilized in therapy, therefore substantiating the clinical feasibility of the RTmon technique.

Nevertheless, it remains to be proven in a forthcoming study whether non symmetric and non homogeneous targets yield these same conclusions. In addition, it also remains to be proven which of the various morphological modifications may be detected with this technique and to which level. Preliminary results obtained already with a simulated anthropomorphic phantom show some of the potentialities of RTmon for assisting radiotherapy [30].

## ACKNOWLEDGMENT

The authors acknowledge the support from the staff of milipeia, the high performance computing cluster of the University of Coimbra (P. Almeida, L. Pinto, and Prof. P. Vieira Alberto); and from LIP (Prof. M. Oliveira and J. Silva).

## REFERENCES

[1] C. Thieke, U. Malsch, W. Schlegel, J. Debus, P. Huber, and R. Bendl *et al.*, "Kilovoltage CT using a linac-CT scanner combination," *Br. J. Radiol.*, vol. 79, pp. 79–86, 2006.

[2] R. de Crevoisier, S. L. Tucker, L. Dong, R. Mohan, R. Cheung, and J. D. Cox *et al.*, "Increased risk of biochemical and local failure in patients with distended rectum on the planning CT for prostate cancer radiotherapy," *Int. J. Radiat. Oncol.*, vol. 62, pp. 965–973, 2005.

[3] C. Lee, K. M. Langen, W. Lu, J. Haimerl, E. Schnarr, and K. J. Ruchala *et al.*, "Evaluation of geometric changes of parotid glands during head and neck cancer radiotherapy using daily MVCT and automatic deformable registration," *Radiother. Oncol.*, vol. 89, pp. 81–88, 2008.

[4] R. Serduc, Y. van de Looij, G. Francony, O. Verdonck, B. van der Sanden, and J. Laissue *et al.*, "Characterization and quantification of cerebral edema induced by synchrotron x-ray microbeam radiation therapy," *Phys. Med. Biol.*, vol. 53, pp. 1153–1166, 2008.

[5] F. Sterzing, R. Engenhart-Cabillic, M. Flentje, and J. Debus, "Options of image-guided radiotherapy - a new dimension in radiation oncology," *Dtsch. Arztebl. Int.*, vol. 108, no. 16, pp. 274–80, 2011.

[6] P. M. Evans, "Anatomical imaging for radiotherapy," *Phys. Med. Biol.*, vol. 53, pp. R151–R191, 2008.

[7] B. Sorcini and A. Tilikidis, "Clinical application of image-guided radiotherapy, IGRT (on the Varian OBI platform)," *Cancer Radiother.*, vol. 10, pp. 252–257, 2006.

[8] D. A. Jaffray, "Emergent technologies for 3-dimensional image-guided radiation delivery," *Semin. Radiat. Oncol.*, vol. 15, no. 3, pp. 208–216, 2005.

[9] W. van Elmpt, L. McDermott, S. Nijsten, M. Wendling, P. Lambin, and B. Mijnheer, "A literature review of electronic portal imaging for radiotherapy dosimetry," *Radiother. Oncol.*, vol. 88, no. 3, pp. 289–309, 2008.

[10] R. de Crevoisier, D. Kuban, and D. Lefkopoulos, "Image-guided radiotherapy by in-room CT-linear accelerator combination," *Cancer Radiother.*, vol. 10, no. 5, pp. 245–251, 2006.

[11] D. Verellen, M. De Ridder, and G. Storme, "A (short) history of image-guided radiotherapy," *Radiother. Oncol.*, vol. 86, pp. 4–13, 2008.

[12] L. N. McDermott, M. Wendling, J. Nijkamp, A. Mans, J.-J. Sonke, and B. Mijnheer *et al.*, "3D in vivo dose verification of entire hypo-fractionated IMRT treatments using an EPID and cone-beam CT," *Radiother. Oncol.*, vol. 86, no. 1, pp. 35–42, 2008.

[13] S. M. Nijsten, B. J. Mijnheer, and A. L. Dekker, "Routine individualized patient dosimetry using electronic portal imaging devices," *Radiother. Oncol.*, vol. 83, no. 1, pp. 65–75, 2007.

[14] J. J. Lagendijk, B. W. Raaymakers, A. J. Raaijmakers, J. Overweg, K. J. Brown, and E. M. Kerkhof *et al.*, "MRI/linac integration," *Radiother. Oncol.*, vol. 86, no. 1, pp. 25–29, 2008.

[15] B. W. Raaymakers, J. J. Wlagendijk, and J. Overweg, "Integrating a 1.5 T MRI scanner with a 6 MV accelerator: Proof of concept," *Phys. Med. Biol.*, vol. 54, pp. 229–237, 2009.

[16] R. George, V. Ramakrishnan, J. V. Siebers, T. D. Chung, and P. J. Keall, "Investigation of patient, tumour and treatment variables affecting residual motion for respiratory-gated radiotherapy," *Phys. Med. Biol.*, vol. 51, no. 20, pp. 5305–5319, 2006.

[17] J.-P. Bissonnette, K. N. Franks, D. J. M. T. G. Purdie, and D. A. J. J.-J. Sonke *et al.*, "Quantifying interfraction and intrafraction tumor motion in lung stereotactic body radiotherapy using respiratory-correlated cone beam computed tomography," *Int. J. Radiat. Oncol. Biol. Phys.*, vol. 75, no. 3, pp. 688–695, 2009.

[18] A. Sawant, R. L. Smith, R. B. Venkat, L. Santanam, B. Cho, and P. Poulsen *et al.*, "Toward submillimeter accuracy in the management of intrafraction motion: The integration of real-time internal position monitoring and multileaf collimator target tracking," *Int. J. Radiat. Oncol. Biol. Phys.*, vol. 74, no. 2, pp. 575–582, 2009.

[19] S. Janek, R. Svensson, C. Jonsson, and A. Brahme, "Development of dose delivery verification by PET imaging of photonuclear reactions following high energy photon therapy," *Phys. Med. Biol.*, vol. 51, no. 22, pp. 5769–5783, 2006.

[20] T. T. Farmer and M. P. Collins, "A new approach to the determination of anatomical cross-sections of the body by Compton scattering of gamma rays," *Phys. Med. Biol.*, vol. 16, pp. 577–586, 1971.

[21] A. Del Guerra, R. Bellazzini, G. Tonelli, R. Venturi, and W. Nelson, "A detailed Monte Carlo study of multiple scattering contamination in Compton tomography at 90 degrees," *IEEE Trans. Med. Imag.*, vol. TMI-1, pp. 147–152, 1982.

[22] G. Harding, "X-ray scatter tomography for explosive detection," *Radiat. Phys. Chem.*, vol. 71, pp. 869–882, 2004.

[23] S. Agostinelli, J. Allison, K. Amako, J. Apostolakis, and H. Araujo *et al.*, "Geant4: A simulation toolkit," *Nucl. Instrum. Meth. A*, vol. 506, no. 3, pp. 250–303, 2003.

[24] J. Allison, K. Amako, J. Apostolakis, H. Araujo, and P. Dubois *et al.*, "Geant4 developments and applications," *IEEE Trans. Nucl. Sci.*, vol. 53, no. 1, pp. 270–8, 2006.

[25] F. Verhaegen and J. Seuntjens, "Monte Carlo modelling of external radiotherapy photons beams," *Phys. Med. Biol.*, vol. 48, pp. R107–R164, 2003.

[26] B. Bednarz and X. G. Xu, "Monte Carlo modeling of a 6 and 18 MV Varian Clinac medical accelerator for in-field and out-of-field dose calculations: Development and validation," *Phys. Med. Biol.*, vol. 54, pp. N43–N57, 2009.

[27] D. L. Gunter, "Collimator design for nuclear medicine," in *Emission Tomography: The Fundamentals of PET and SPECT*. Waltham, MA, USA: Elsevier Inc., 2004, ch. 8.

[28] The R Project for Statistical Computing [Online]. Available: http://www.rproject.org/

[29] H. Simões, M. Pinto, M. Cunha, J. Gonçalves, L. Sampaio, and R. J. Ferreira *et al.*, "Dose-free monitoring of radiotherapy treatments with scattered photons: First experimental results at a 6-MV linac," *IEEE Trans. Nucl. Sci.*, to be published.

[30] M. C. Battaglia, H. Simões, V. Bellini, E. Cisbani, M. C. Lopes, and P. Crespo, "Orthogonal ray imaging with megavoltage beams: Simulated results with an anthropomorphic phantom," in *Conf. Records IEEE Nucl. Sci. Symp. & Med. Imag. Conf. (NSS/MIC)*, Anaheim, CA, USA, Oct. 27–Nov. 3 2012, M22-6.